Equivalence Principle Violation in Vainshtein Screened Two-Body Systems

Takashi Hiramatsu[1], Wayne Hu[2], Kazuya Koyama[3] and Fabian Schmidt[4]

[1] *Yukawa Institute for Theoretical Physics, Kyoto University, Kyoto 606-8502, Japan*
[2] *Kavli Institute for Cosmological Physics, Department of Astronomy & Astrophysics, University of Chicago, Chicago IL 60637*
[3] *Institute of Cosmology & Gravitation, University of Portsmouth,*
Dennis Sciama Building, Portsmouth, PO1 3FX, UK
[4] *California Institute of Technology, Mail Code 350-17, Pasadena, CA, 91125*

In massive gravity, galileon, and braneworld explanations of cosmic acceleration, force modifications are screened by nonlinear derivative self-interactions of the scalar field mediating that force. Interactions between the field of a central body ("A") and an orbiting body ("B") imply that body B does not move as a test body in the field of body A if the orbit is smaller than the Vainshtein radius of body B. We find through numerical solutions of the joint field at the position of B that the A-field Laplacian is nearly perfectly screened by the B self-field, whereas first derivative or net forces are reduced in a manner that scales with the mass ratio of the bodies as $(M_B/M_A)^{3/5}$. The latter causes mass-dependent reductions in the universal perihelion precession rate, with deviations for the Earth-Moon system at the $\sim 4\%$ level. In spite of universal coupling, which preserves the microscopic equivalence principle, the motion of macroscopic screened bodies depends on their mass providing in principle a means for testing the Vainshtein mechanism.

PACS numbers: 98.80.-k

arXiv:1209.3364v1 [hep-th] 15 Sep 2012

I. INTRODUCTION

The current acceleration of the cosmic expansion is one of the most puzzling aspects of modern cosmology. Aside from a cosmological constant whose smallness remains unexplained, the simplest models typically involve an additional scalar field either implicitly or explicitly. Universal coupling of this field to matter would produce gravitational strength fifth forces and naively be excluded by laboratory and solar system bounds. Viable models must therefore implement a so-called screening mechanism to hide fifth forces locally.

Screening mechanisms invoke nonlinearity in the field equations to change the nature of the fifth force in high density regions. For example, the chameleon mechanism increases the mass of the field in deep gravitational potentials [1] whereas the symmetron mechanism changes its coupling to matter [2]. A third possibility is the Vainshtein mechanism [3, 4], first introduced in the context of massive gravity to suppress the propagation of additional helicity modes [5, 6]. Here nonlinear derivative interactions of the field act to screen the fifth force within the so-called Vainshtein radius around a matter source. The Vainshtein mechanism occurs not only in modern incarnations of Boulware-Deser [7] ghost-free massive gravity [8–11] but also in galileon cosmology [12–18] and braneworld models. Indeed it is in the braneworld model of Dvali, Gabadadze and Porrati (DGP) [19] that it has been best studied [20–26].

Interestingly, these mechanisms are distinguished by how screened bodies fall in external fields [27]. As a consequence of universal coupling, all unscreened test bodies fall in the same way and obey a microscopic equivalence principle. In the chameleon and symmetron models, screened bodies do not respond to external fields. In the Vainshtein mechanism they do, but only if those fields have wavelengths long compared to the Vainshtein radius. These differences arise because the self-field of the screened body and the external field do not in general superimpose but rather interfere in a manner dependent on the nonlinear interaction [28].

In this paper, we consider the Vainshtein mechanism in the near-field limit. In particular we study the motion of two bodies which are separated by much less than their individual Vainshtein radii and look for apparent violations of the equivalence principle. The two-body problem is particularly relevant since it has been shown that for the orbit of test bodies, there is a universal anomalous precession rate induced by a Vainshtein-screened scalar field that is potentially measurable in next generation solar system tests of General Relativity [21, 29]. However in the Earth-Moon system the Moon is screened on scales out to nearly a parsec for cosmologically motivated models and cannot be considered as a test body in the Earth's field. In principle, this nonlinearity can affect the interpretation of lunar ranging tests for anomalous precession and more generally lead to results that depend on the nature of the orbiting body. To understand this system, the field must be solved jointly in the presence of both sources. For definiteness, we will implement the Vainshtein mechanism in the DGP model but our results readily apply to the galileon and massive gravity incarnations as well.

The remainder of the paper is organized as follows. We briefly review the Vainshtein mechanism and the spherically-symmetric one-body solution in Sec. II. In Sec. III, we discuss violation of the superposition principle in the two-body case. We present numerical results and their scaling with the two-body parameters in Sec. IV. Details of the numerical scheme is given in Appendix A. We discuss the implications of these results in Sec. V.

II. VAINSHTEIN MECHANISM

A. DGP example

As an example of models that accommodate the Vainshtein mechanism, we consider the DGP braneworld model [19]. In the DGP model, there is a dynamical degree of freedom representing the bending of the brane embedded in the five-dimensional bulk which we denote $\phi(\mathbf{x}, t)$. In the quasi-static limit where its time-derivatives can be neglected, its equation of motion becomes [21, 23]

$$3\beta(t)\frac{\nabla^2}{a^2}\phi + \frac{1}{a^4}N[\phi,\phi] = 8\pi G\delta\rho, \tag{1}$$

where

$$\beta(t) = 1 \pm 2Hr_c\left(1 + \frac{\dot{H}}{3H^2}\right), \tag{2}$$

$$N[\phi_A,\phi_B] = r_c^2(\nabla^2\phi_A\nabla^2\phi_B - \nabla_i\nabla_j\phi_A\nabla^i\nabla^j\phi_B), \tag{3}$$

and $\delta\rho = \rho - \bar{\rho}$, the density fluctuation from the cosmic mean. Spatial derivatives here are in comoving coordinates. The key parameter in this model is the crossover scale

$$r_c = \frac{G_5}{2G}, \tag{4}$$

the ratio between the five dimensional Newton constant G_5 and the four dimensional one G.

The + sign in $\beta(t)$ corresponds to the normal branch solution while the − sign corresponds to the self-accelerating solution. In this paper, we only consider the solutions with $\beta > 0$ since $\beta < 0$ is associated with ghost instabilities [30]. Furthermore, since we are interested in static solutions at the current epoch $a = 1$, we set $\beta = 1$. All results can be rescaled to the general β case by replacing r_c with $r_c/\sqrt{\beta}$ and densities $\delta\rho$ with $\delta\rho/\beta$, or equivalently the masses of all bodies.

We have written the nonlinear operator $N[\phi_A, \phi_B]$ in bilinear form allowing for two separate fields since in the two body calculation that follows it will be useful to consider the interference between the two individual fields. It is the nonlinearity of this operator that is responsible for both the Vainshtein mechanism and the lack of a superposition principle for the brane bending mode.

B. One Body Solution

The Vainshtein mechanism and the scale associated with it can be illustrated with simple analytic one-body solutions. For a spherically symmetric object with a top-hat constant density, the scalar field equation (1) reduces to

$$3\left(\frac{d^2\phi}{dR^2} + \frac{2}{R}\frac{d\phi}{dR}\right) + r_c^2\left[\frac{2}{R^2}\left(\frac{d\phi}{dR}\right)^2 + \frac{4}{R}\frac{d^2\phi}{dR^2}\frac{d\phi}{dR}\right] = 8\pi G\delta\rho, \tag{5}$$

where the top-hat density profile is

$$\delta\rho(R) = \begin{cases}\delta\rho_0 & R \le r_s \\ 0 & R > r_s\end{cases}, \tag{6}$$

with r_s as the radius of the source. Eq. (5) can be integrated by multiplying both sides by R^2dR , resulting in

$$3R^2\frac{d\phi}{dR} + 2Rr_c^2\left(\frac{d\phi}{dR}\right)^2 = 8\pi G\int_0^R \delta\rho(R')R'^2\,dR' = \begin{cases}8\pi G\delta\rho_0 R^3/3 & R \le r_s, \\ 8\pi G\delta\rho_0 r_s^3/3 & R > r_s.\end{cases} \tag{7}$$

As this is a quadratic equation for $d\phi/dR$ we immediately obtain

$$\frac{d\phi}{dR} = \frac{3R}{4r_c^2} \times \begin{cases} g(r_s) & R \le r_s, \\ g(R) & R > r_s, \end{cases} \tag{8}$$

where

$$g(R) = \sqrt{1 + \left(\frac{r_*}{R}\right)^3} - 1, \quad r_* = \left(\frac{8r_g r_c^2}{9}\right)^{1/3}, \tag{9}$$

and the Schwarzschild radius

$$r_g = 2GM = \frac{8\pi G}{3}\delta\rho_0 r_s^3. \tag{10}$$

The radius r_* is called the *Vainshtein radius*. For $r_s < R \ll r_*$, we obtain $g(R) \propto R^{-3/2}$, so $\phi(R) \propto R^{1/2}$ +const. This means that for test bodies the correction to Newtonian forces around the source vanishes in the limit $r_s \ll r_*$, and thus Einstein gravity is recovered [22]. This condition is satisfied if $r_g \gg 9r_s^3/(8r_c^2)$ which is the case for stars and even the Earth and the Moon as long as we set r_c to be a cosmological scale. Equivalently, for spherically symmetric systems the Vainshtein mechanism is active whenever the mean enclosed overdensity $3M/4\pi R^3$ is greater than

$$\rho_{\rm th} = \frac{9}{8(H_0 r_c)^2}\rho_{\rm cr}, \tag{11}$$

where $\rho_{\rm cr}$ is the critical density.

We can in fact obtain the full solution for ϕ in closed form [26]. For $R \ge r_s$, defining $x \equiv R/r_*$ and $A = 3r_*^2/(4r_c^2)$, we can express the solution of Eq. (8) in terms of the hypergeometric function,

$$\phi_{\rm ex}(x) = C_1 + \frac{A}{2}f(x), \qquad \text{for } x \ge x_s, \tag{12}$$

where C_1 is an integral constant, $x_s \equiv r_s/r_*$, and

$$f(x) \equiv x^2\left[{}_2F_1\left(-\frac{1}{2}, -\frac{2}{3}; \frac{1}{3}; -\frac{1}{x^3}\right) - 1\right]. \tag{13}$$

On the other hand, in the internal region, $R < r_s$, the solution of Eq. (8) is

$$\phi_{\rm in}(x) = \frac{A}{2}x^2 g(x_s) + C_2, \qquad \text{for } x < x_s. \tag{14}$$

Note that in this case, the two pieces of the nonlinear terms combine and imply

$$\left[(\nabla^2\phi_{\rm in})^2 - (\nabla_i\nabla_j\phi_{\rm in})^2\right] = \frac{2}{3}(\nabla^2\phi_{\rm in})^2. \tag{15}$$

More generally, for any ϕ_A

$$N[\phi_A, \phi_{\rm in}] = \frac{2}{3}r_c^2\nabla^2\phi_A\nabla^2\phi_{\rm in}. \tag{16}$$

This relation is specific to the interior of a top hat $\phi_{\rm in}$ but nonetheless will be useful when approximating the nonlinear term.

The inner and external solutions should be continuous at $x = x_s$. Without loss of generality, we can take $C_1 = 0$ due to the shift symmetry of the scalar field equation of motion. Then we obtain the solution for a single source, $\phi(x) = \phi_{\rm in}(x)\Theta(x_s - x) + \phi_{\rm ex}(x)\Theta(x - x_s)$ with

$$\phi_{\rm ex}(x) = \frac{A}{2}f(x), \quad \phi_{\rm in}(x) = \frac{A}{2}\left[f(x_s) + g(x_s)(x^2 - x_s^2)\right]. \tag{17}$$

For $R \ll r_*$ and $r_s \ll r_*$, these solutions can be approximated as

$$\begin{aligned} \phi_{\rm ex}(R) &\approx \frac{\sqrt{2}r_g^{1/2}}{r_c}R^{1/2} + A\frac{\Gamma[-2/3]\Gamma[7/6]}{\sqrt{\pi}}, \\ \phi_{\rm in}(R) &\approx \frac{r_g^{1/2}}{2\sqrt{2}r_c r_s^{3/2}}R^2 + \frac{3r_g^{1/2}r_s^{1/2}}{2\sqrt{2}r_c} + A\frac{\Gamma[-2/3]\Gamma[7/6]}{\sqrt{\pi}}, \end{aligned} \tag{18}$$

with a Laplacian of

$$\nabla^2\phi_{\rm ex}(R) = \frac{3r_g^{1/2}}{2\sqrt{2}r_c}R^{-3/2}, \quad \nabla^2\phi_{\rm in}(R) = \frac{3r_g^{1/2}}{\sqrt{2}r_c r_s^{3/2}}. \tag{19}$$

That the radial dependence of these solutions is proportional to $r_g^{1/2} \propto M^{1/2}$ is an indication that mass sources do not linearly superimpose within the Vainshtein radius. On the other hand in the opposite limit of $R \gg r_* \gg r_s$,

$$\phi(R) \approx -\frac{r_g}{3R}\left(1 - \frac{r_g r_c^2}{18R^3}\right). \tag{20}$$

Leading order linearity in $r_g \propto M$ implies that mass sources do superimpose in this limit. Since the leading order term in the Laplacian $\nabla^2\phi = 0$, residual effects go as

$$\nabla^2\phi(R) \approx \frac{2}{9}\frac{r_g^2 r_c^2}{R^6}. \tag{21}$$

These approximate forms will be useful in constructing scaling relations and boundary conditions for the two body problem.

III. TWO BODY PROBLEM

The brane bending field of a single body derived in the previous section suffices to study the motion of test particles around that body. For test particles, there is a universal anomalous precession rate, dependent only on the crossover scale r_c, that can be used to test the Vainshtein mechanism [21, 29]. However for most realistic orbiting bodies, their own Vainshtein radius is too large for them to be considered test particles. This is in particular true for the Earth-Moon system where the orbit of the Moon is well within its own Vainshtein radius.

Through the nonlinearity of the Vainshtein effect, the orbiting body's self-field interferes with that of the central body and can in principle affect its orbit. Indeed the scaling of the single body field as $\sqrt{M}$ is an indication of the non-superimposability of solutions within the Vainshtein radius. Two sources will add as $\sqrt{M_A + M_B}$ for distances from the center of mass much larger than the separation.

In this section, we consider a two-body problem such as the Earth-Moon system to study non-superimposability of solutions. We begin in §III A with the parameterization of the two body system in terms of the physical scales in the problem. We describe how screening operates directly on second derivatives of the field and indirectly on first derivatives, or average forces in §III B. We examine the geometry of screening in §III C and introduce our screening statistics and their scaling properties in §III D.

A. Model Parameters

Given spherically symmetric masses, the system has axial symmetry and so we use cylindrical coordinates (r, θ, z). We assume that the two bodies, denoted as A and B, are separated from each other by d, and they are located at $(r, z) = (0, 0)$ for body A and $(r, z) = (0, -d)$ for body B. We denote their respective Schwarzschild and physical radii as r_{gA}, r_{gB} and r_{sA}, r_{sB}. In the following we assume body A is heavier than body B. The schematic illustration of the two-body set up is shown in Fig. 1.

In our numerical solutions below, we choose parameters that reflect the Earth ("E") and Moon ("M") where possible. In the actual Earth-Moon system $d = 3.8\times10^5$ km and choosing $r_c \sim cH_0^{-1}$ as appropriate for cosmologically-motivated models would require an 10^8 dynamic range between the Vainshtein radius of the Earth and the separation d since

$$\frac{cH_0^{-1}}{d} = 3.3 \times 10^{17}\left(\frac{0.73}{h}\right). \tag{22}$$

Furthermore between the separation scale d and the body radii are several more orders of magnitude

$$\begin{aligned} r_{sE} &= 6378\,\text{km} = 1.7 \times 10^{-2} d, \\ r_{sM} &= 1737\,\text{km} = 4.6 \times 10^{-3} d. \end{aligned} \tag{23}$$

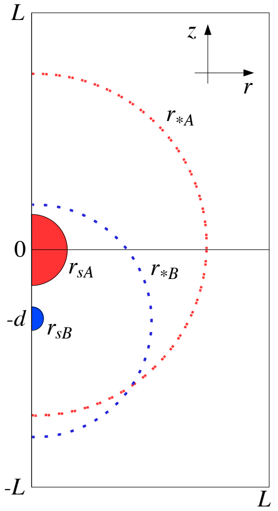

FIG. 1: Schematic illustration of the two body problem (not drawn to scale). Physical radii are shown by the solid lines whereas the Vainshtein radii, r_{*A} and r_{*B} are shown in dashed lines. Boundary conditions are set at $r = L$ and $z = \pm L$ with vanishing deviations from superposition of A and B.

On the other hand, we shall see that the most important properties of the two body solution can be expressed as a function of the mass ratio M_B/M_A, whereas other properties can be inferred by examining the scalings of results with r_c/d and r_s/d.

Our fiducial choice will therefore be to take d and masses, or equivalently Schwarzschild radii, from the Earth-Moon system

$$\begin{aligned}\frac{r_{gA}}{d} &= 2\frac{GM_{\rm E}}{d} = 2.3 \times 10^{-11},\\ \frac{r_{gB}}{d} &\equiv 2\frac{GM_{\rm M}}{d} = \frac{r_{gA}}{d}\left(\frac{M_M}{M_E}\right).\end{aligned} \tag{24}$$

Since we are interested in effects around body B we fix $r_{sA}/d = 0.3$ and explore the dependence on r_{sB}. Likewise we explore the dependence of results on r_c/d. Our fiducial choices for these parameters are listed in Table. I.

M_B/M_A	1/80
r_{gA}/d	2.3×10^{-11}
r_c/d	10^8
r_{sA}/d	0.3
r_{sB}/d	0.1
r_{gB}/d	2.8×10^{-13}
r_{*A}/d	58.91
r_{*B}/d	13.67
L/d	286.7
h/d	0.0125

TABLE I: The fiducial parameters for the two-body problem where M_B/M_A and r_{gA}/d mimic the Earth-Moon system. The top set represents the primary parameters whose individual variation we explore below. The middle set represents derived parameters. The last two parameters are numerical and give the box and grid size (see Appendix A).

It is useful both numerically and analytically to express the two body problem in terms of deviations from the superposition principle. Denoting the full solution as

$$\phi = \phi_A + \phi_B + \phi_\Delta, \tag{25}$$

where ϕ_A and ϕ_B are the solutions to the single body equations, the field equation for the deviation ϕ_Δ is

$$3\nabla^2\phi_\Delta + N[\phi_\Delta, \phi_\Delta] + 2N[\phi_A + \phi_B, \phi_\Delta] = -2N[\phi_A, \phi_B]. \tag{26}$$

The interference term $N[\phi_A, \phi_B]$ can be considered as the source of deviations from superposition.

We solve Eq. (26) numerically with boundary conditions

$$\phi_\Delta(L, z) = \phi_\Delta(r, -L) = \phi_\Delta(r, L) = 0, \tag{27}$$

corresponding to the case $L \gg r_{*A}$ where we can superpose single-body solutions. Finally the equations are solved by finite difference on an inhomogeneous grid with minimum spacing h/d (see Appendix A).

B. Screening

Before turning to numerical solutions of the two body system it is useful to examine the structure of Eq. (26) and develop an analytic intuition for the results. In particular, Eq. (26) admits screening solutions where the field of body B suppresses some aspect of the field of body A around itself and vice versa.

To see this screening behavior note that both $\phi_\Delta = -\phi_A$ and $\phi_\Delta = -\phi_B$ are solutions to this equation *outside* of the sources where $3\nabla^2\phi_{A,B} + N[\phi_{A,B}, \phi_{A,B}] = 0$. In particular, around body B we might expect $\phi_\Delta = -\phi_A$ such that it cancels the effect of body A. However these source-free solutions would not match the boundary conditions at the sources themselves and so what occurs in reality is more complicated.

Screening really occurs in the second derivatives of the field. Note that we are also free to add a pure gradient to any of these source-free solutions, e.g.

$$\phi_\Delta = -\phi_A + \mathbf{C}\cdot\mathbf{x} + D \tag{28}$$

and still solve the equations. Thus we might expect that screening operates by replacing ϕ_A with a version of itself that is linearized over some region of influence around body B that can be much larger than the physical size of the body (cf. [27]).

We start with the simple expectations from approximating the nonlinear term with the Laplacian in Eq. (16). In this approximation the more general screening expectation becomes

$$\nabla^2\phi_\Delta \approx \begin{cases} -\nabla^2\phi_A, & \nabla^2\phi_B \gg \nabla^2\phi_A \\ -\nabla^2\phi_B, & \nabla^2\phi_B \ll \nabla^2\phi_A \end{cases}, \tag{29}$$

with the constants $\mathbf{C}$ and D providing the appropriate matching of the regimes. Note that if ϕ_A is already nearly linear around body B, as is the case for a distant source [27] we expect no self-field effect on the motion of body B. On the other hand we know that there must be a near field effect on forces between the bodies: without screening the force from body A on body B

$$F_{AB} \propto M_B\sqrt{M_A}, \tag{30}$$

whereas that from body B on body A

$$F_{BA} \propto -M_A\sqrt{M_B}. \tag{31}$$

This violation of Newton's third law would cause momentum non-conservation in the joint system.

To get a rough sense for the size and scaling of near field effects we can replace $\phi_A \propto \sqrt{R}$ with a linearization of itself across the region on the z-axis where $\nabla^2\phi_B > \nabla^2\phi_A$

$$\left|\frac{z_{\rm min}}{d}\right| = \frac{1}{1 + (M_B/M_A)^{1/3}}, \quad \left|\frac{z_{\rm max}}{d}\right| = \frac{1}{1 - (M_B/M_A)^{1/3}}, \tag{32}$$

or

$$\phi_\Delta(0, z) = -\phi_A(0, z) + \frac{\phi_A(0, z_{\rm max}) - \phi_A(0, z_{\rm min})}{z_{\rm max} - z_{\rm min}}(z - z_{\rm min}) + \phi_A(0, z_{\rm min}). \tag{33}$$

In this crude approximation, the gradient $\partial_z\phi_A(0, -d)$ is reduced by

$$\frac{\partial_z\phi_\Delta}{\partial_z\phi_A}(0, -d) \sim -\frac{3}{8}\left(\frac{M_B}{M_A}\right)^{2/3} + \mathcal{O}\left(\frac{M_B}{M_A}\right)^{4/3}. \tag{34}$$

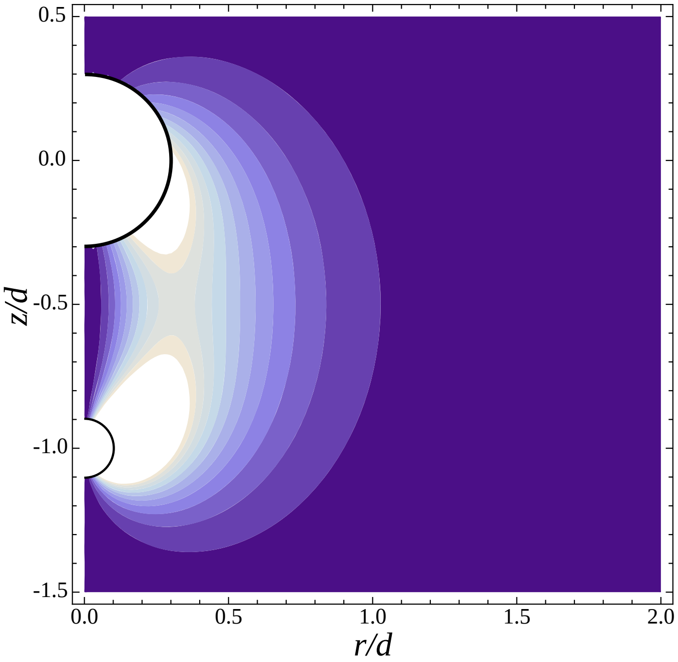

FIG. 2: Two-body nonlinearity source function $F[r/d, z/d] \propto N[\phi_A, \phi_B]$ with A at $(0, 0)$ and B at $(0, -1)$ with parameters of the fiducial model (see Tab. I). The region interior to the bodies, within the semicircles, is not shown.

independently of the physical size of the bodies and the value of $r_c/d \gg 1$. For the Earth-Moon mass ratio this is a $\sim 2\%$ correction of the gradient even though the second derivative is screened across a much larger range, $\Delta z/d \sim 0.5$, than the physical size of the Moon $\Delta z/d \sim 0.005$. Nonetheless the dependence on the mass ratio represents an apparent violation of the equivalence principle.

Note that momentum conservation in the joint system would imply that at body A there is near complete screening of the force from body B

$$\frac{\partial_z \phi_\Delta}{\partial_z \phi_B}(0,0) \approx -1 + \sqrt{\frac{M_B}{M_A}} \left[1 + \frac{\partial_z \phi_\Delta}{\partial_z \phi_A}(0,-d) \right] \tag{35}$$

for $r_{sA}, r_{sB} \ll d$. As a check of our numerical results we will examine

$$\frac{F_{AB}}{F_{BA}} = \frac{M_B}{M_A} \frac{(\partial_z \phi_A + \partial_z \phi_\Delta)\,|_{0,-d}}{(\partial_z \phi_B + \partial_z \phi_\Delta)\,|_{0,0}} \tag{36}$$

to determine how well Newton's third law $F_{BA}/F_{AB} = -1$ is satisfied.

Note that in the opposite limit $d \ll r \ll r_{A*}$, where the sources add as $\sqrt{M_A + M_B}$, we know that the field of body A screens that of body B more directly. The ϕ_Δ field here is simply the difference between the joint and individual sources

$$\phi_\Delta \propto \sqrt{M_A + M_B} - \sqrt{M_A} - \sqrt{M_B} \approx -\sqrt{M_B}, \tag{37}$$

for $M_B \ll M_A$ implying

$$\phi_\Delta \approx -\phi_B. \tag{38}$$

While these considerations provide a qualitative guide to results, the specific form of the second derivatives in $N[\phi_A, \phi_B]$ lead to important consequences for the geometry of the screening around body B which we shall now consider.

C. Toroidal Geometry

In order to understand the geometry of screening around body B, let us examine the source to the ϕ_Δ field in Eq. (26)

$$2N[\phi_A,\phi_B] = \frac{9}{2} r_c^2 \frac{\sqrt{GM_A}\sqrt{GM_B}}{d^3} F[r/d, z/d], \tag{39}$$

where the geometry is determined by a universal function in cylindrical coordinates scaled to the separation d

$$F[\tilde{r},\tilde{z}] = \frac{\tilde{r}^2}{(\tilde{r}^2+\tilde{z}^2)^{7/4}(\tilde{r}^2+(\tilde{z}+1)^2)^{7/4}}. \tag{40}$$

This function is plotted in Fig. 2. Instead of the roughly spherical geometry that the arguments based on the Laplacian would predict, the true interference of the self-field of B on that of A is toroidal around body B. The basic reason for this geometry is that along the z axis the cross terms cancel given the difference structure in Eq. (3).

On the other hand, interior to body B, the nonlinear source becomes

$$2N[\phi_A,\phi_B] = \frac{6r_c^2\sqrt{GM_A}\sqrt{GM_B}}{r_{sB}^{3/2}(r^2+z^2)^{3/4}} \tag{41}$$

and does not vanish for $r = 0$ but rather approaches a constant for $d \gg r_{sB}$. Note that for a small physical size r_{sB}, $r^2 + z^2 \approx d^2$ in the interior. The interference term is nearly constant and approximates an effective density of $\sqrt{\rho_B \rho_{A,\rm eff}}$ where $\rho_{A,\rm eff} = M_A/(4\pi d^3/3)$. Unlike the true density, $2N[\phi_A,\phi_B]$ does not vanish in the exterior but has a jump in value at the r_{sB} boundary. We shall see that this jump causes a similar discontinuity in the second derivatives of ϕ_Δ at the boundary.

Finally, although $2N[\phi_A,\phi_B]$ peaks at the bodies themselves (saturated in Fig. 2), this does not necessarily mean that the relative impact on the joint field peaks there. The single body Laplacians also peak there and we must examine deviations with respect to those fields in the results that follow.

D. Screening Statistics

It is therefore useful to introduce our primary, or Laplacian, screening statistic for the relative impact of the field of body B on that of A

$$Q_2(r,z) = \frac{\nabla^2\phi_\Delta}{\nabla^2\phi_A}. \tag{42}$$

If screening is complete, $Q_2 \to -1$.

It is again useful to derive rough analytic scalings for the screening statistic in various limits. When either A or B dominate in the second derivatives we expect that the second derivatives of the correction field ϕ_Δ is small compared with the dominant one and screens the subdominant one. We therefore expect the field equation (26) to be satisfied approximately by dropping terms nonlinear in ϕ_Δ. Furthermore, the $3\nabla^2\phi_\Delta$ terms is small compared with the nonlinear terms deep within the Vainshtein radius and so

$$N[\phi_A+\phi_B,\phi_\Delta] \approx -N[\phi_A,\phi_B]. \tag{43}$$

We can further approximate the left hand side of Eq. (43) using Eq. (16)

$$N[\phi_A+\phi_B,\phi_\Delta] \approx \frac{2}{3} r_c^2 \nabla^2(\phi_A+\phi_B)\nabla^2\phi_\Delta. \tag{44}$$

This relation is exact only for the interior field and for $\nabla^2\phi_B \gg \nabla^2\phi_A$ but gives a reasonable heuristic description elsewhere. This approximation is useful in that it allows us to solve directly for $\nabla^2\phi_\Delta$, and hence

$$Q_{2\rm in}(r,z) \approx -\left[1+\frac{1}{2}\left(\frac{M_A}{M_B}\right)^{1/2}\left(\frac{r_{sB}^2}{r^2+z^2}\right)^{3/4}\right]^{-1}, \tag{45}$$

$$Q_{2\rm ex}(r,z) \approx -\left\{\frac{3}{2}\frac{d^2r^2}{(r^2+z^2)[r^2+(z+d)^2]}\right\}\left\{1+\left(\frac{M_A}{M_B}\right)^{1/2}\left[\frac{r^2+(z+d)^2}{r^2+z^2}\right]^{3/4}\right\}^{-1}. \tag{46}$$

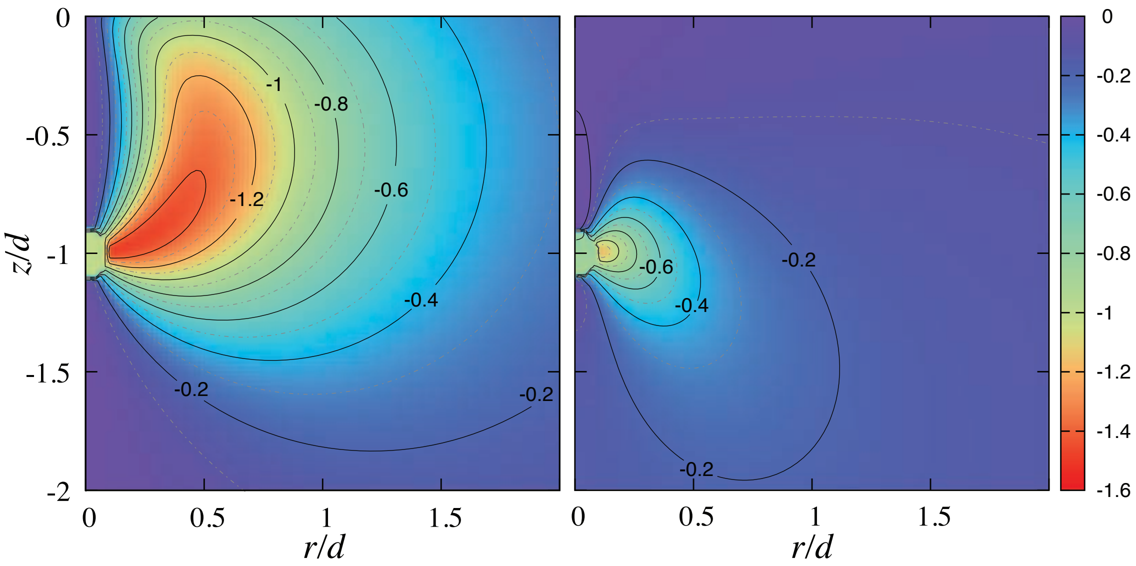

FIG. 3: Laplacian-screening statistic $Q_2 = \nabla^2\phi_\Delta/\nabla^2\phi_A$ (left: analytic; right: numerical). The red areas indicate a large relative deviation from the superposition solution in the Laplacian of the field. In the interior of body B screening of the Laplacian of body A is nearly complete whereas in the exterior there is a toroidal region of mutual screening. The analytic description is in good qualitative agreement near body B. Parameters are the fiducial choice of Tab. I.

The left hand panel in Fig. 3 shows the results of $Q_2(r,z)$ obtained from Eqs. (45) and (46).

In fact for small radius $r \ll d$, we can approximate $r^2 + z^2 \sim d^2$. Then on the $z = -d$ axis, Q_2 is approximately given by

$$Q_{2\rm in}(r,-d) \approx -\left[1 + \frac{1}{2}\left(\frac{M_A}{M_B}\right)^{1/2}\left(\frac{r_{sB}}{d}\right)^{3/2}\right]^{-1}, \tag{47}$$

$$Q_{2\rm ex}(r,-d) \approx -\frac{3}{2}\left[1 + \left(\frac{M_A}{M_B}\right)^{1/2}\left(\frac{r}{d}\right)^{3/2}\right]^{-1}, \tag{48}$$

Note that saturation to $Q_2 = -1$ in the interior increases with increasing M_B/M_A and decreasing r_{sB} as expected from the fact that the interior value of $\nabla^2\phi_B$ scales with these parameters. We can infer from this scaling that for realistic situations where $r_{sB} \ll d$ (see Eq. 23), that $Q_2 \approx -1$ for any $M_B < M_A$. At the body surface, there is a jump to a maximum value of $-3/2$. We shall see from numerical results that this maximum value is only approximate since Eq. (44) is not strictly valid in this limit.

Nonetheless, the qualitative aspects of Q_2 indicate that the impact on forces is as a redistribution of force changes across a toroidal region around body B rather than a linearization across a quasi-spherical one. Since the volume of the regions are comparable, we expect the scaling behavior of Eq. (34) to be roughly satisfied. To quantify this expectation, we define the force-screening statistic

$$Q_1(r) = \frac{\partial_z\phi_\Delta}{\partial_z\phi_A}\Big|_{z=-d}. \tag{49}$$

Note that along $z = -d$ the gradient of the ϕ_B field is along the r-direction and hence its screening does not contribute to Q_1. Again if screening of forces from ϕ_A is complete then $Q_1 \to -1$.

For distances $R = \sqrt{r^2 + z^2}$ from the bodies that are large compared with the separation d, Eq. (37) and (21) imply

$$Q_2 \approx \begin{cases} -\sqrt{\frac{M_B}{M_A}}, & d \ll R \ll r_{*A} \\ 2\frac{M_B}{M_A}, & R \gg r_{*A} \end{cases}, \tag{50}$$

which will also be useful in checking our numerical results. In particular, Q_2 does not depend explicitly on r_c aside from setting the transition scale r_{*A}. In the $R \gg r_{*A}$ regime this independence is due to the vanishing of $\nabla^2\phi_A$ to leading order. Other statistics do not share this independence. To see the more general dependence on r_c note that the field equation for deviations from superposition Eq. (26) only has no explicit r_c dependence when the nonlinear terms dominate

$$N[\phi_\Delta,\phi_\Delta]+2N[\phi_A+\phi_B,\phi_\Delta]\approx -2N[\phi_A,\phi_B] \tag{51}$$

and hence fractional effects of ϕ_Δ relative to ϕ_A or ϕ_B have no r_c dependence. To see when this approximation is valid, take the opposite $r_c\to 0$ limit. In that case,

$$3\nabla^2\phi_\Delta \approx -2N[\phi_A,\phi_B]\propto r_c^2, \qquad r_c\to 0. \tag{52}$$

The linear and non-linear terms in Eq. (26) become comparable when

$$\max(r_c^2\nabla_i\nabla_j\phi_B, r_c^2\nabla_i\nabla_j\phi_A)\approx 1 \tag{53}$$

which occurs for the typical distance d around the bodies when $r_{*A}\approx d$. Once $r_{*B}\gg d$, Eq. (51) becomes valid and all statistics lose their dependence on r_c around the bodies.

IV. RESULTS

In this section we present numerical solutions to the full nonlinear equation and scaling relations based on them. The details of numerical calculations are presented in Appendix A.

We begin by considering the fiducial parameter choices from Tab. I. In Fig. 3 (right) we show a 2D contour plot of the Laplacian-screening statistic Q_2 of Eq. (42). As expected from the analytic argument of the previous section, $Q_2\approx -1$ interior to body B indicating nearly full screening. At the surface of the body, it experiences a jump to $Q_2<-1$ which then extends to a toroidal region around the body. In this toroidal region, where the individual body

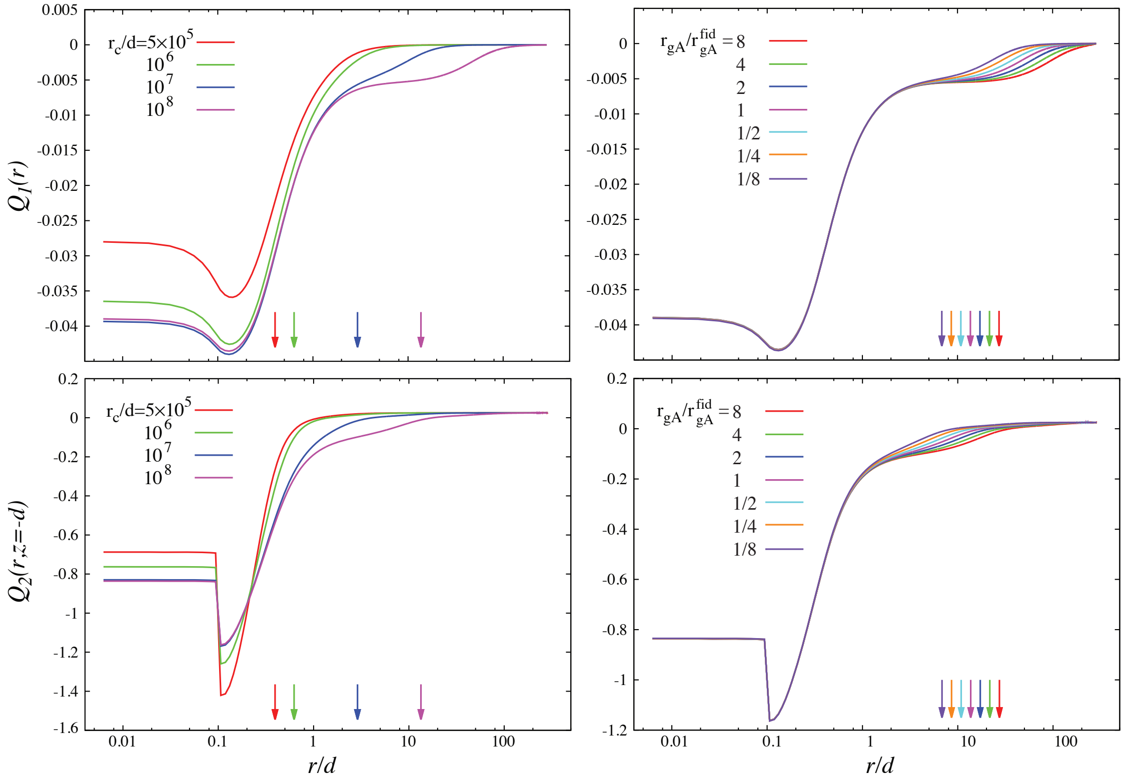

FIG. 4: Force (Q_1, top) and Laplacian (Q_2, bottom) screening statistics along $z=-d$ as a function of the crossover scale r_c (left) and absolute mass scale $r_{gA}=2GM_A$ (right). Other parameters including M_B/M_A are set to the fiducial choices of Tab. I here and in the following figures. Arrows indicate the Vainshtein scale of body B, r_{*B}. Near the body the screening statistics are independent of r_c and mass scale if $r_{*B}\gg d$.

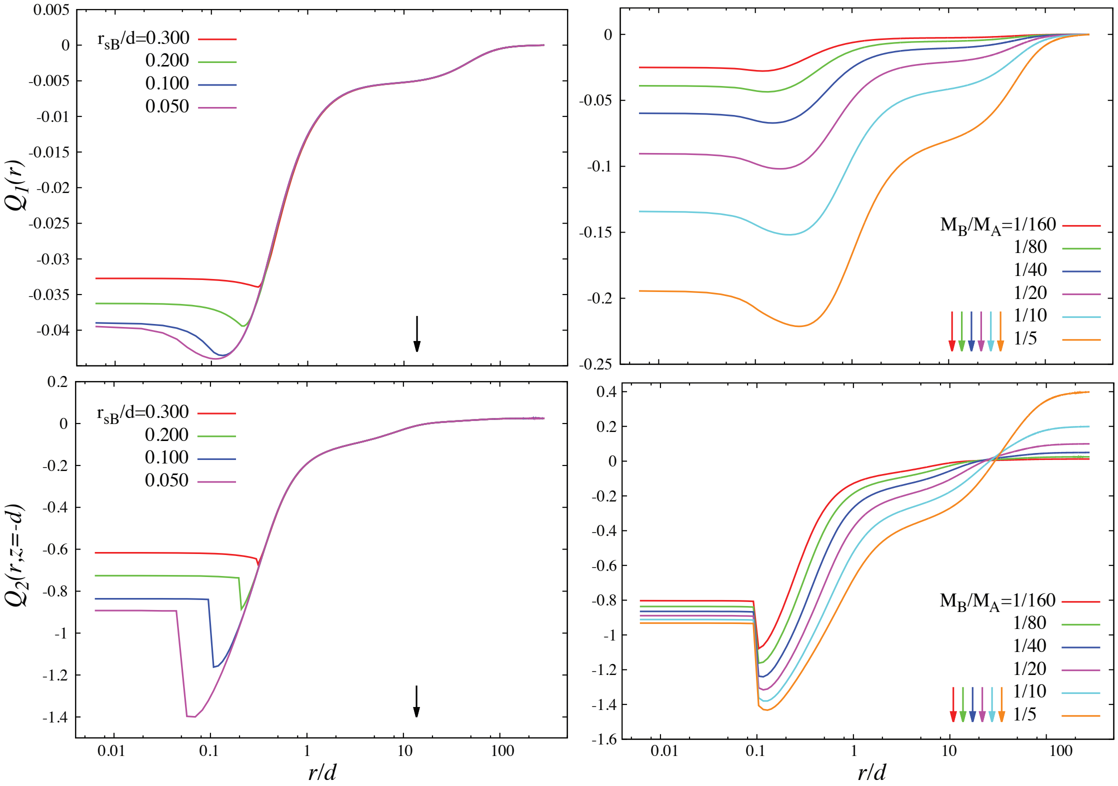

FIG. 5: Screening statistics as a function of the size of body B r_{sB} (left) and mass ratio M_B/M_A (right) as in Fig. 4. Q_1 and Q_2 are independent of r_{sB} in the exterior $r > r_{sB}$ and converge to constant values for $r < r_{sB} \ll d$. Likewise for M_B/M_A, Q_2 behaves according to analytic expectations for $r \gg d$ and both Q_1 and Q_2 scale with the mass ratio in the interior $r < r_{sB} = 0.1$.

Laplacians are comparable, Q_2 quantifies both the screening effect of B on A and A on B. Comparison with Fig. 3 (left) shows that our crude analytic approximation of Eq. (48) captures many of the qualitative effects around body B.

To isolate the effect of screening of B on A, it is useful to examine the force-screening statistic Q_1 of Eq. (49). The field of B is purely radial around B and Q_1 measures the change in the gradient along the z-direction. As shown in Fig. 4 (top), Q_1 increases toward body B and then smoothly approaches a constant in the interior of the body. For this Earth-Moon like system $Q_1(0) \approx -0.04$ or approximately double the crude expectation from Eq. (34). The more dramatic changes in Q_2 (see Fig. 4, bottom) reflect changes in the radial structure of the joint field.

The fiducial parameter choices reflect a crossover scale r_c/d that is much smaller than the actual Earth-Moon system, a coupling strength β set to unity by rescaling the masses r_g/d, and body sizes r_s/d that are large compared with the separation. We therefore next test the dependence of our results on these parameters before turning to the central dependence on the mass ratio M_B/M_A.

In Fig. 4 (left), we show the dependence of the force and Laplacian screening statistics on r_c/d. For $r_c \ll 10^7 d$, the screening statistics scales strongly with r_c as expected from Eq. (52). This behavior saturates once $r_{*B} \gg d$. In Fig. 4, we show the r_{*B} value corresponding to r_c with an arrow. Indeed so long as $r_c \gg 10^7 d$ or equivalently $r_{*B} \gg d$ the results for both are insensitive to r_c near body B. As expected from Eq. (50), for large r_c/d there is an interval $d \ll r \ll r_{*A}$ where $Q_2 \approx -\sqrt{M_B/M_A}$. For $r \gtrsim r_{*A}$, $Q_2 \approx 2M_B/M_A$ verifying that we have taken a sufficiently large L that the boundary condition $\phi_\Delta = 0$ is appropriate (see Appendix A 5 for an explicit test).

In Fig. 4 (right), we show the dependence on the absolute mass scale or r_{gA}/d at fixed M_B/M_A and other fiducial parameters. Recall that changing the mass scale can also be interpreted as changing the parameter β in the original field equation (1). The only dependence of results on the mass scale is through its effect on the Vainshtein scales and in the external far field limit relative to the separation d.

Next we consider the impact of the physical size of body B, r_{sB} in Fig. 5 (left). As r_{sB} shrinks, Q_2 interior to the body approaches -1. This is expected from our analytic expression, Eq. (48), due to the fact that the maximum value that $\nabla^2\phi_B$ attains is controlled by r_{sB}. Once $\nabla^2\phi_B \gg \nabla^2\phi_A$ in the interior we expect results to become independent of r_{sB}. For the fiducial parameters, Q_2 has not quite saturated whereas in Q_1 it has almost reached its asymptotic value by $r_{sB}/d = 0.1$. In the exterior of body B, Q_2 drops increasingly below -1 as r_{sB}/d decreases. This large overshoot is not reflected in Q_1 and hence represents the screening of the radial body B field itself. Again since the maximum $\nabla^2\phi_B$ increases as r_{sB} decreases, $\nabla^2\phi_\Delta$ increases relative to the constant $\nabla^2\phi_A$ as well for the screening of the B field. Since statistics in the exterior of body B do not depend on its size, there is likewise no dependence on the size of body A, r_{sA} exterior to A.

We conclude that in the limit of $r_c/d \gg 1$ and $r_{sB}/d \ll 1$, the main dependence of the screening variables on the system parameters is through the mass ratio M_B/M_A. This dependence is shown in Fig. 5 (right). For Q_2 interior to body B, raising the ratio increases the efficacy of screening body A as expected from Eq. (45). In the exterior, it increases the overshooting effect, also as expected. For Q_1, screening in the interior scales strongly with the mass ratio as expected from Eq. (34). In both cases, in the far field limit $r \gg d$, results scale according to the analytic expectations of Eq. (37), (21), and Eq. (50) to excellent approximation.

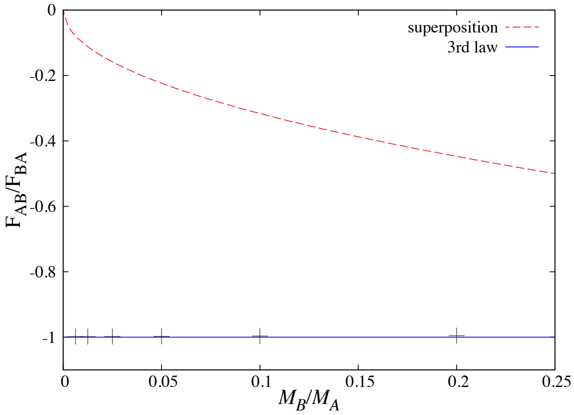

FIG. 6: Test of Newton's third law or momentum conservation. If the fields of A and B superimposed, then the ratio of forces would be $-\sqrt{M_B/M_A}$ (red dashed line) and violate the third law (solid blue line). Numerical results (+ points) show that the joint solution restores the third law through violation of the superposition principle $\phi_\Delta \neq 0$.

As shown in Fig. 6, these results for Q_1 near body B are exactly what is required to restore Newton's third law and momentum conservation [see Eq. (36)]. Had the two fields superimposed, then the force ratio would be $-\sqrt{M_B/M_A}$ whereas our numerical results are consistent with -1.

While our analytic approximations provide a qualitative description of our results, near body B the geometry of the screening inhibits their accuracy. It is therefore useful to quantify Q_1 and Q_2 with empirical fits at the center of body B. For Q_1, the numerical results can be described by a scaling relation similar to Eq. (34) but with a finite size correction (see Fig. 7)

$$Q_1(0) \approx -0.56\left(\frac{M_B}{M_A}\right)^{0.6}\left[1 - 0.13\left(\frac{M_A}{M_B}\right)^{1/2}\left(\frac{r_{sB}}{d}\right)^{3/2}\right], \tag{54}$$

for $M_B/M_A \lesssim 0.1$ and when the correction in brackets is small. In particular, we can extrapolate this fit to the physically interesting limit where $r_{sB}/d \ll 1$, $Q_1(0) \approx -0.56(M_B/M_A)^{0.6}$.

For Q_2, our results are consistent with approaching -1 in the physically relevant limit

$$Q_2(0,-d) \approx -1 + 0.23\left(\frac{r_{sB}}{d}\right)^{0.74}\left(\frac{M_B}{M_A}\right)^{-0.32}. \tag{55}$$

In practice, the approach is somewhat slower than that predicted by Eq. (45) due primarily to inaccuracy in the replacement of second derivatives with Laplacians in Eq. (44). Nonetheless if we extrapolate Eq. (55) to the true Earth-Moon system where $r_{sB}/d = 0.0046$ the correction from full screening $Q_2 = -1$ remains only at the percent level.

V. DISCUSSION

In this paper we studied the apparent violation of the equivalence principle in a model with the Vainshtein mechanism where nonlinear derivative interactions of the field act to screen the fifth force. We considered the motion of two

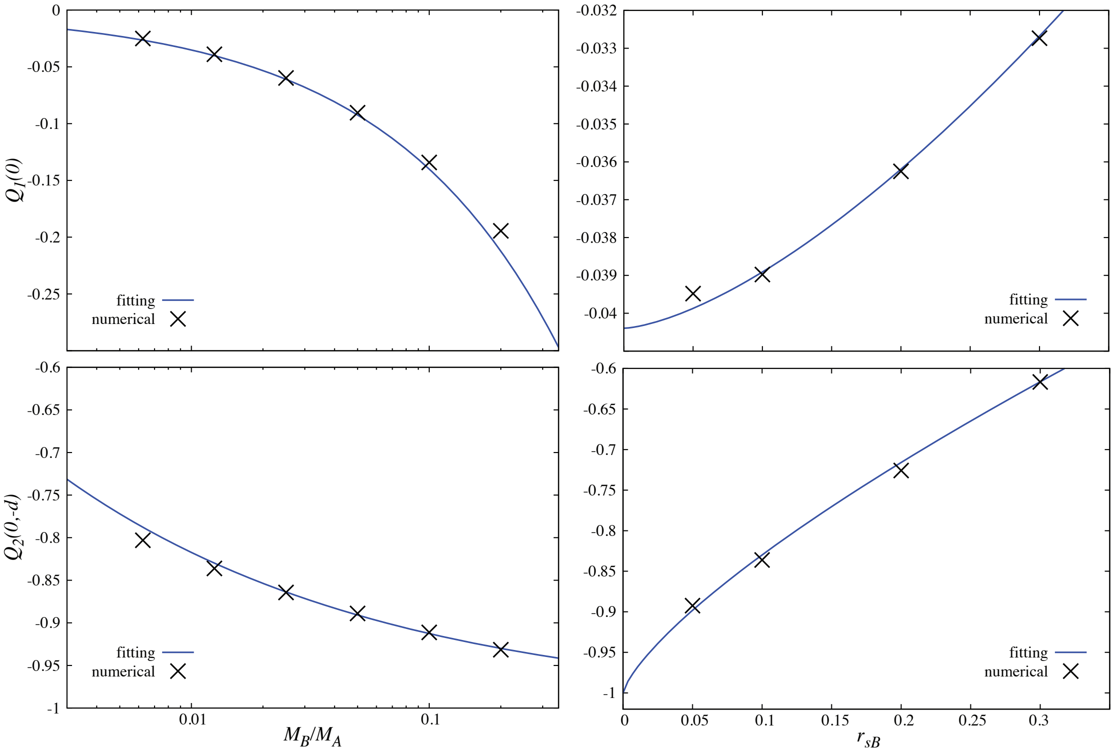

FIG. 7: Screening statistics at the center of body B, $Q_1(0)$ and $Q_2(0,-d)$ for various r_{sB} and M_B/M_A with other parameters held fixed to fiducial values. We show numerical results as points ($\times$) as well as the fitting functions in Eqs. (54) and (55).

bodies which are separated by much less than their individual Vainshtein radii such as the Earth-Moon system. In such a system, the small body B cannot be considered as a test body in the large body A's field ϕ_A. The nonlinear equation for the field allows for screening solutions where the Laplacian of ϕ_A is screened within a region much larger in extent than the physical size of body B. The primary effect is that the Laplacian $\nabla^2\phi_A$ is fully screened. A crude estimate of the residual impact on the first derivatives or forces would suggest a suppression of order $(M_B/M_A)^{2/3}$ where M_B/M_A is the mass ratio of the two bodies. Moreover, in the limit where the Vainshtein radii $r_{*A,B}$ are much larger than the separation d between the two bodies, we expect relative screening effects to be independent of the crossover scale r_c.

We confirmed these qualitative expectations by solving the joint two body system numerically. Cast in terms of the deviation of the true field from the superposition solution $\phi_\Delta = \phi - \phi_A - \phi_B$, in the interior of body B there is nearly full screening $\nabla^2\phi_\Delta \approx -\nabla^2\phi_A$ in the limit that the size of body B is much smaller than the separation between the bodies. On the other hand, the screening of forces from the large body on the small body depend almost exclusively on the mass ratio M_B/M_A. From numerical solutions, we found it is given by $Q_1(0) \approx -0.56(M_B/M_A)^{0.6}$.

The fifth force introduces an additional contribution to the anomalous perihelion precession rate. In the DGP normal branch, the precession rate was obtained by ignoring the non-superimposability and treating the small body (e.g., Moon) as a test body. The precession rate (the angle of perihelion advanve $\Delta\varphi_{\rm DGP}$ during one orbital period P) is universal under this assumption and given by

$$\frac{\Delta\varphi_{\rm DGP}}{P} = \frac{3}{8}\frac{1}{r_c} = 7.91\left(\frac{h}{H_0 r_c}\right)\mu\text{arcsec/yr}. \tag{56}$$

This result needs to be revisited in the light of our finding. As screening operates by replacing the large body's field with a linearized version of itself, one might think that this affects the precession rate qualitatively by changing the radial dependence of the force law. However, the fractional effect is independent of the separation d and the impact of non-superimposability comes from the field at the position of the small body B, not at a fixed r. Then the only effect of screening is to reduce the large body's force by the factor of $1 + Q_1$ and we have a proportional change in the precession,

$$\frac{\Delta\varphi_{\rm DGP}}{P} = \frac{3}{8}\frac{1}{r_c}(1 + Q_1). \tag{57}$$

Precession thus depends on the mass ratio of the bodies and is not universal. Different mass bodies will precess at different rates leading to an apparent equivalence principle violation. On the other hand, the mass ratio scaling of the equivalence principle violation implies that for typical systems the effect will be small. For example, for the mass ratio of the Earth-Moon system $M_B/M_A = 1/80$, leading to a small deviation (4%) from the universal precession rate. Nonetheless, in principle the Vainshtein mechanism can be tested by precision tests of the perihelion precession of different mass objects.

Acknowledgments

We thank Alexander Belikov and Y. Suwa for useful discussions. TH was supported by JSPS Grant-in-Aid for Young Scientists (B) No.23740186, partially by JSPS Grant-in-Aid for Scientific Research (A) No.21244033, and also by MEXT HPCI STRATEGIC PROGRAM. WH was supported by U.S. Dept. of Energy contract DE-FG02-90ER-40560, the Kavli Institute for Cosmological Physics at the University of Chicago through grants NSF PHY-0114422 and NSF PHY-0551142 and an endowment from the Kavli Foundation and its founder Fred Kavli, and the David and Lucile Packard Foundation. KK was supported by STFC grantST/H002774/1, the ERC and the Leverhulme trust. FS was supported by the Gordon and Betty Moore Foundation at Caltech. WH, KK, FS thank the Aspen Center for Physics where this project was initiated and the organizers of the Ringberg dark energy meeting where it was completed. KK thanks the Kavli Institute for Cosmological Physics at the University of Chicago for its hospitality.

Appendix A: Numerical Techniques

1. Cylindrical Coordinates

The field equation for the two-body deviation from superposition ϕ_Δ given by Eq. (26) has cylindrical symmetry along the z-axis separating the bodies (see Fig. 1) and so

$$\begin{aligned}&\left[1+\frac{2r_c^2}{3}\left(\frac{1}{r}\frac{\partial\phi_{AB}}{\partial r}+\frac{\partial^2\phi_{AB}}{\partial z^2}\right)\right]\frac{\partial^2\phi_\Delta}{\partial r^2}+\left[1+\frac{2r_c^2}{3}\left(\frac{1}{r}\frac{\partial\phi_{AB}}{\partial r}+\frac{\partial^2\phi_{AB}}{\partial r^2}\right)\right]\frac{\partial^2\phi_\Delta}{\partial z^2}\\&+\left[1+\frac{2r_c^2}{3}\left(\frac{\partial^2\phi_{AB}}{\partial r^2}+\frac{\partial^2\phi_{AB}}{\partial z^2}\right)\right]\frac{1}{r}\frac{\partial\phi_\Delta}{\partial r}-\frac{4r_c^2}{3}\frac{\partial^2\phi_{AB}}{\partial r\partial z}\frac{\partial^2\phi_\Delta}{\partial r\partial z}+\frac{1}{3}N[\phi_\Delta,\phi_\Delta]=-\frac{2}{3}N[\phi_A,\phi_B],\end{aligned}\tag{A1}$$

where $\phi_{AB}=\phi_A+\phi_B$ and we have used

$$\nabla^2\phi_a=\frac{\partial^2\phi_a}{\partial r^2}+\frac{1}{r}\frac{\partial\phi_a}{\partial r}+\frac{\partial^2\phi_a}{\partial z^2},\tag{A2}$$

and

$$\begin{aligned}\frac{1}{r_c^2}N[\phi_a,\phi_b]=&\frac{1}{r}\left(\frac{\partial\phi_a}{\partial r}\frac{\partial^2\phi_b}{\partial r^2}+\frac{\partial^2\phi_a}{\partial r^2}\frac{\partial\phi_b}{\partial r}\right)-2\frac{\partial^2\phi_a}{\partial r\partial z}\frac{\partial^2\phi_b}{\partial r\partial z}\\&+\left(\frac{\partial^2\phi_a}{\partial r^2}+\frac{1}{r}\frac{\partial\phi_a}{\partial r}\right)\frac{\partial^2\phi_b}{\partial z^2}+\frac{\partial^2\phi_a}{\partial z^2}\left(\frac{\partial^2\phi_b}{\partial r^2}+\frac{1}{r}\frac{\partial\phi_b}{\partial r}\right),\end{aligned}\tag{A3}$$

where $\phi_a,\phi_b\in\{\phi_A,\phi_B,\phi_{AB},\phi_\Delta\}$. We treat r_{gA}/d, M_B/M_A, r_{sA}/d, r_{sB}/d and r_c/d as the model parameters as mentioned in Sec. III A and so our fundamental unit of length is the separation d.

In our numerical computations, we impose the regularity condition at $r=0$, given as $\partial\phi/\partial r=0$. As for the other boundaries, we assume that superposition holds; namely, we set $\phi_\Delta=0$ at the exterior boundaries. We study the effects of the finite computational domain on the numerical solution in Appendix A 5.

2. Nonlinear Coordinates

To justify the assumption, $\phi_\Delta=0$ at the boundaries, we have to use a box size $L\gg r_{*A}$. However, we also want $r_{*B}\gg d$ and so it is quite difficult to simulate these conditions in the (r,z) coordinate choice.

Since high resolution is only required near the bodies, we can extend the dynamic range with the help of a nonlinear transformation of the radial and axial variables

$$r=\rho+\frac{\alpha}{3}\rho^3,\quad z=\zeta+\frac{\alpha}{3}\zeta^3,\tag{A4}$$

where α is a constant controlling the growth of the grid spacing at large distance. According to these equations, the spatial intervals in the original coordinate are given by

$$\begin{aligned}\frac{\Delta r}{\Delta\rho} &\equiv A^{-1}(\rho) = (1+\alpha\rho^2),\\ \frac{\Delta z}{\Delta\zeta} &\equiv B^{-1}(\zeta) = (1+\alpha\zeta^2),\end{aligned} \tag{A5}$$

becoming large at large distance for fixed $\Delta\rho$ and $\Delta\zeta$ relative to the finer resolution at the origin. If we take $\alpha = 0.1$, $\rho = 20d$ corresponds to $r \approx 286.7d$. Since $r_{*A}/d = 58.9$, this choice satisfies our requirement, $r_{*A} \ll L$, and we take it as the fiducial size of the computational domain (see Table I).

In these rescaled coordinates, Eqs. (A 1) and (A3) are further transformed according to

$$\frac{\partial\phi}{\partial r} = A\frac{\partial\phi}{\partial\rho}, \quad \frac{\partial^2\phi}{\partial r^2} = A^2\frac{\partial^2\phi}{\partial\rho^2} + AA'\frac{\partial\phi}{\partial\rho}, \tag{A6}$$

$$\frac{\partial\phi}{\partial z} = B\frac{\partial\phi}{\partial\zeta}, \quad \frac{\partial^2\phi}{\partial z^2} = B^2\frac{\partial^2\phi}{\partial\zeta^2} + BB'\frac{\partial\phi}{\partial\zeta}, \quad \frac{\partial^2\phi}{\partial r\partial z} = AB\frac{\partial^2\phi}{\partial\rho\partial\zeta}. \tag{A7}$$

3. Discretization

We discretize the computational domain as $\rho_i = (i+1/2)h$ and $\zeta_j = (j-N)h$ with $i = 0, 1, \ldots, N$ and $j = 0, 1, \ldots, 2N$ where h is the spatial interval. Note that since

$$L = (Nh) + \frac{\alpha}{3}(Nh)^3, \tag{A8}$$

the fiducial parameter choices of Tab. I are achieved with $\alpha = 0.1$ and $N = 1600$.

The derivatives with respect to ρ and ζ are approximated by the central finite differences on the grid as

$$\begin{aligned}\frac{\partial\phi}{\partial\rho} &\approx \frac{\phi_{i+1,j}-\phi_{i-1,j}}{2h}, & \frac{\partial^2\phi}{\partial\rho\partial\zeta} &\approx \frac{\phi_{i+1,j+1}-\phi_{i-1,j+1}-\phi_{i+1,j-1}+\phi_{i-1,j-1}}{4h^2},\\ \frac{\partial^2\phi}{\partial\rho^2} &\approx \frac{\phi_{i+1,j}-2\phi_{i,j}+\phi_{i-1,j}}{h^2}, & \frac{\partial^2\phi}{\partial\zeta^2} &\approx \frac{\phi_{i,j+1}-2\phi_{i,j}+\phi_{i,j-1}}{h^2},\end{aligned} \tag{A9}$$

where we abbreviated $\phi_{i,j} = \phi(\rho_i, \zeta_j)$. The reason why we shift the ρ coordinate by half a spatial interval h is to be able to easily impose the Neumann boundary condition at $\rho = 0$. Considering an auxiliary point at $i = -1$, the boundary condition reads

$$\left.\frac{\partial\phi}{\partial\rho}\right|_{\rho=0} = 0 \quad\Longrightarrow\quad \frac{\phi_{0,j}-\phi_{-1,j}}{h} = 0, \quad \therefore \phi_{-1,j} = \phi_{0,j}. \tag{A10}$$

Thus the boundary condition for the value of the auxiliary point enforces the vanishing of the derivative without modifying the finite difference scheme. For example, the radial term in the Laplacian evaluated at $i = 0$ becomes

$$\begin{aligned}\left.\left\{A^2\frac{\partial^2\phi}{\partial\rho^2} + \left(AA' + \frac{A}{r}\right)\frac{\partial\phi}{\partial\rho}\right\}\right|_{\rho=\rho_0} &\approx A^2\frac{\phi_{1,j}-2\phi_{0,j}+\phi_{-1,j}}{h^2} + \left(AA' + \frac{A}{r}\right)\frac{\phi_{1,j}-\phi_{-1,j}}{2h}\\ &= A^2\frac{\phi_{1,j}-\phi_{0,j}}{h^2} + \left(AA' + \frac{A}{r}\right)\frac{\phi_{1,j}-\phi_{0,j}}{2h}.\end{aligned} \tag{A11}$$

Equation (A1) written in (ρ, ζ) coordinate can then be recast as a matrix equation, schematically given as

$$(\text{linear terms of } \phi_\Delta) = N[\phi_\Delta, \phi_\Delta] + N[\phi_A, \phi_B] \quad\longrightarrow\quad A\mathbf{x} = \widetilde{\mathbf{b}} \equiv \mathbf{f}(\mathbf{x}) + \mathbf{b}, \tag{A12}$$

where the matrix A represents the discrete linear operators on ϕ given by the combination of Eq. (A9), being an asymmetric 9-band sparse $(N+1)(2N+1) \times (N+1)(2N+1)$ matrix, and $\mathbf{b}$ and $\mathbf{f}$ are vectors containing $N[\phi_A, \phi_B]$ and $[\phi_\Delta, \phi_\Delta]$ evaluated at (ρ_i, ζ_j).

4. Iteration scheme

To solve the set of nonlinear equations given in Eq. (A12), we use a combination of preconditioned Conjugate Gradient Squared (CGS) and Successive Over-Relaxation (SOR) methods according to Ref. [31]. Let the n-th iterated solution be $\mathbf{x}^{(n)}$. We evaluate the right-hand side of Eq. (A12), $\widetilde{\mathbf{b}}^{(n)} = \mathbf{b} + \mathbf{f}(\mathbf{x}^{(n)})$. Then we solve the linear equation, $A\mathbf{x}^* = \widetilde{\mathbf{b}}^{(n)}$, by CGS. Finally, we update the solution $\mathbf{x}^{(n+1)}$ by SOR as

$$\mathbf{x}^{(n+1)} = \omega \mathbf{x}^* + (1-\omega)\mathbf{x}^{(n)}, \tag{A13}$$

where we set $\omega = 0.5 \sim 1$ to make the iterative solution converge.

To achieve the fast convergence of CGS, we precondition the matrix A with modified incomplete LU (MILU) decomposition, referred to as MILUCGS in the literature. We decompose A such that $A = LDU + R$, where L, U are just the copies of lower and upper triangular part of A, and D is a diagonal matrix, which are given by

$$L_{ij} = \begin{cases} 0 & i<j \\ d_i^{-1} & i=j \\ A_{ij} & i>j \end{cases}, \quad U_{ij} = \begin{cases} A_{ij} & i<j \\ d_i^{-1} & i=j \\ 0 & i>j \end{cases}, \quad D_{ij} = d_i \delta_{ij}. \tag{A14}$$

The diagonal element d_i is recursively calculated by

$$\begin{aligned} d_i^{-1} = A_{ii} &- A_{i,i-N} d_{i-N}(A_{i-N,i} + A_{i-N,i-N+1}) \\ &- A_{i,i-1} d_{i-1}(A_{i-1,i} + A_{i-1,i+N-1}), \end{aligned}$$

Multiplying $(LDU)^{-1}$ in both sides in Eq. (A12), we obtain a new operator matrix $A' = (LDU)^{-1}A = I + (LDU)^{-1}R$ where we formally separated as $A = LDU + R$. The resultant matrix A' becomes close to a unit matrix in the sense that the weight of the non-zero components of A' becomes significant near the diagonal. In other words, the condition number $\kappa(A') = ||A'^{-1}||/||A'||$ becomes small. This treatment is frequently used to accelerate the convergence of CGS.

We stop the SOR iteration in Eq. (A13) if we achieve

$$\frac{||\widetilde{\mathbf{b}}^{(n+1)} - A\mathbf{x}^{(n+1)}||}{||\widetilde{\mathbf{b}}^{(n+1)}||} < \epsilon_{\rm SOR}, \tag{A15}$$

where $||\cdots||$ represents the standard 2-norm, and we set $\epsilon_{\rm SOR} = 10^{-8}$.

5. Convergence Tests

First, we show the accuracy of our numerical results when we take the fiducial choice of parameters. In Fig. 8, we plot the ratio of the residuals of the field equation (26) to its source term,

$$\epsilon_{\rm err}(r,z) \equiv \frac{3\nabla^2\phi_\Delta + N[\phi_\Delta,\phi_\Delta] + 2N[\phi_A+\phi_B,\phi_\Delta] + 2N[\phi_A,\phi_B]}{2N[\phi_A,\phi_B]}. \tag{A16}$$

Setting $\epsilon_{\rm SOR} = 10^{-8}$, we find that the local residuals along $z=-d$ are suppressed to less than 10^{-6} except in the far-field regime where they are still below 10^{-4}. Recall that the boundary conditions at the edges of the box are set to enforce superposition. Given finite computational resources there is a trade-off between increased box size and central resolution.

We therefore also test robustness of our results to the box size L and resolution h. In Fig. 9 (top), we vary α at fixed h or N thus changing L. As long as $L \gg r_{*B}$ results near the body are independent of box size. If $L > r_{*A}$ then we regain the far-field behavior, justifying the use of superposition boundary conditions. In Fig. 9 (bottom), we study resolution h by changing N at fixed α. Interior to body B, a resolution of $h/r_{sB} \leq 0.125$ is required to obtain converged results.

---

[1] J. Khoury and A. Weltman, Phys.Rev. **D69**, 044026 (2004), astro-ph/0309411.

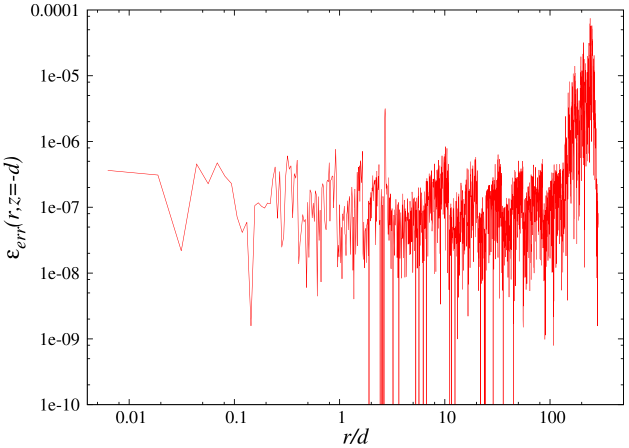

FIG. 8: The fractional accuracy of the numerical results with the fiducial choice of parameters along $z = -d$.

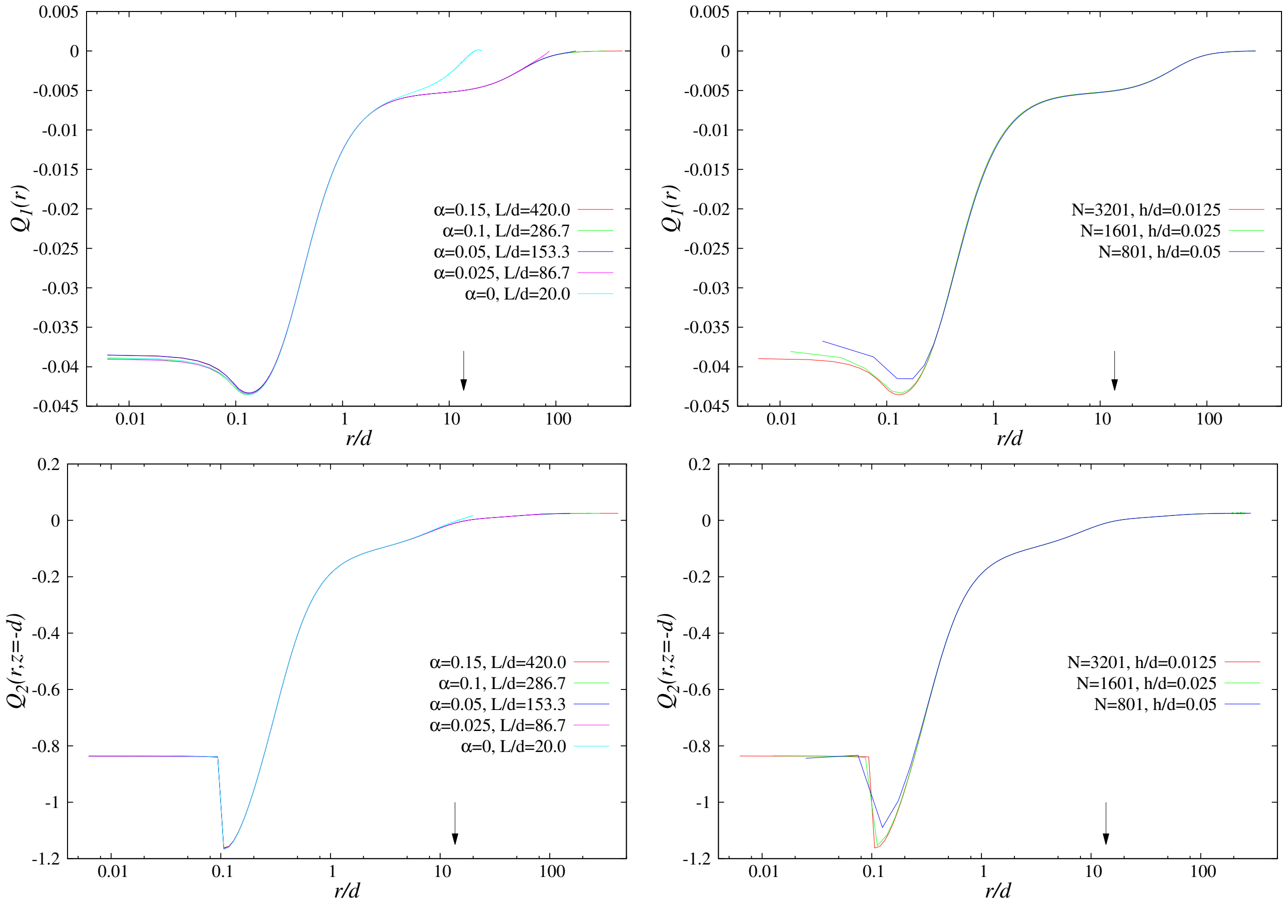

FIG. 9: Box size and resolution dependence of screening statistics. Left: changing α at fixed N, h changes the box size L. Results are independent of L near the bodies if $L \gg r_{*B}$ (arrows). Right: changing N at fixed α changes the resolution h. Results are independent of h if $h \ll r_{sB}$.

[2] K. Hinterbichler and J. Khoury, Phys.Rev.Lett. **104**, 231301 (2010), 1001.4525.
[3] A. Vainshtein, Phys.Lett. **B39**, 393 (1972).
[4] E. Babichev, C. Deffayet, and R. Ziour, Phys.Rev. **D82**, 104008 (2010), 1007.4506.
[5] H. van Dam and M. Veltman, Nucl.Phys. **B22**, 397 (1970).
[6] V. Zakharov, JETP Lett. **12**, 312 (1970).

[7] D. Boulware and S. Deser, Phys.Lett. **B40**, 227 (1972).
[8] C. de Rham, G. Gabadadze, and A. J. Tolley, Phys.Rev.Lett. **106**, 231101 (2011), 1011.1232.
[9] G. Chkareuli and D. Pirtskhalava, Phys.Lett. **B713**, 99 (2012), 1105.1783.
[10] K. Koyama, G. Niz, and G. Tasinato, Phys.Rev. **D84**, 064033 (2011), 1104.2143.
[11] F. Sbisa, G. Niz, K. Koyama, and G. Tasinato, Phys.Rev. **D86**, 024033 (2012), 1204.1193.
[12] A. Nicolis, R. Rattazzi, and E. Trincherini, Phys.Rev. **D79**, 064036 (2009), 0811.2197.
[13] C. Deffayet, G. Esposito-Farese, and A. Vikman, Phys.Rev. **D79**, 084003 (2009), 0901.1314.
[14] C. Burrage and D. Seery, JCAP **1008**, 011 (2010), 1005.1927.
[15] N. Kaloper, A. Padilla, and N. Tanahashi, JHEP **1110**, 148 (2011), 1106.4827.
[16] A. De Felice, R. Kase, and S. Tsujikawa, Phys.Rev. **D85**, 044059 (2012), 1111.5090.
[17] R. Kimura, T. Kobayashi, and K. Yamamoto, Phys.Rev. **D85**, 024023 (2012), 1111.6749.
[18] C. de Rham, A. J. Tolley, and D. H. Wesley (2012), 1208.0580.
[19] G. Dvali, G. Gabadadze, and M. Porrati, Phys.Lett. **B485**, 208 (2000), hep-th/0005016.
[20] C. Deffayet, G. Dvali, G. Gabadadze, and A. I. Vainshtein, Phys.Rev. **D65**, 044026 (2002), hep-th/0106001.
[21] A. Lue and G. Starkman, Phys.Rev. **D67**, 064002 (2003), astro-ph/0212083.
[22] A. Lue, R. Scoccimarro, and G. D. Starkman, Phys.Rev. **D69**, 124015 (2004), astro-ph/0401515.
[23] K. Koyama and F. P. Silva, Phys.Rev. **D75**, 084040 (2007), hep-th/0702169.
[24] F. Schmidt, Phys.Rev. **D80**, 043001 (2009), 0905.0858.
[25] F. Schmidt, Phys.Rev. **D80**, 123003 (2009), 0910.0235.
[26] F. Schmidt, W. Hu, and M. Lima, Phys.Rev. **D81**, 063005 (2010), 0911.5178.
[27] L. Hui, A. Nicolis, and C. Stubbs, Phys.Rev. **D80**, 104002 (2009), 0905.2966.
[28] W. Hu, Nucl.Phys.Proc.Suppl. **194**, 230 (2009), 0906.2024.
[29] G. Dvali, A. Gruzinov, and M. Zaldarriaga, Phys.Rev. **D68**, 024012 (2003), hep-ph/0212069.
[30] K. Koyama, Class.Quant.Grav. **24**, R231 (2007), 0709.2399.
[31] M. Shibata, Phys.Rev. **D55**, 2002 (1997).